











# High-throughput multimodal wide-field Fourier-transform Raman microscope

B. ARDINI,<sup>1</sup> A. BASSI,<sup>1</sup>  A. CANDEO,<sup>1</sup>  A. GENCO,<sup>1</sup> C. TROVATELLO,<sup>2</sup>  F. LIU,<sup>3,4</sup>  X. ZHU,<sup>3</sup> G. VALENTINI,<sup>1,5</sup>  G. CERULLO,<sup>1,5</sup>  R. VANNA,<sup>5,6</sup>  AND C. MANZONI<sup>5,\*</sup> 

<sup>1</sup>Dipartimento di Fisica, Politecnico di Milano, Piazza Leonardo da Vinci 32, I-20133 Milano, Italy

<sup>2</sup>Department of Mechanical Engineering, Columbia University, New York, New York 10027, USA

<sup>3</sup>Department of Chemistry, Columbia University, New York, New York 10027, USA

<sup>4</sup>Department of Chemistry, Stanford University, Stanford, California 94305, USA

<sup>5</sup>Istituto di Fotonica e Nanotecnologie, IFN-CNR, Piazza Leonardo da Vinci 32, I-20133 Milano, Italy

<sup>6</sup>renzo.vanna@cnr.it

\*cristianangelo.manzoni@cnr.it

Received 1 March 2023; revised 26 April 2023; accepted 1 May 2023; published 24 May 2023

Raman microscopy is a powerful analytical technique for materials and life sciences that enables mapping the spatial distribution of the chemical composition of a sample. State-of-the-art Raman microscopes, based on point-scanning frequency-domain detection, have long ( $\sim 1$  s) pixel dwell times, making it challenging to acquire images of a significant area (e.g.,  $100 \times 100 \mu\text{m}$ ). Here we present a compact wide-field Raman microscope based on a time-domain Fourier-transform approach, which enables parallel acquisition of the Raman spectra on all pixels of a 2D detector. A common-path birefringent interferometer with exceptional delay stability and reproducibility can rapidly acquire Raman maps ( $\sim 30$  min for a 250 000 pixel image) with high spatial ( $< 1 \mu\text{m}$ ) and spectral ( $\sim 23 \text{ cm}^{-1}$ ) resolutions. Time-domain detection allows us to disentangle fluorescence and Raman signals, which can both be measured separately. We validate the system by Raman imaging plastic microbeads and demonstrate its multimodal operation by capturing fluorescence and Raman maps of a multilayer-WSe<sub>2</sub> sample, providing complementary information on the strain and number of layers of the material. © 2023 Optica Publishing Group under the terms of the [Optica Open Access Publishing Agreement](#)

[Publishing Agreement](#)

<https://doi.org/10.1364/OPTICA.488860>

## 1. INTRODUCTION

Raman scattering (RS) microscopy is a remarkably powerful investigation technique in materials [1] and life sciences [2], as it enables label-free and non-invasive determination of the (bio)chemical composition of a sample. In RS, a monochromatic light beam at frequency  $\nu_0$  irradiates the sample and is inelastically scattered at frequency  $\nu_S(\nu_{AS}) = \nu_0 - (+)\nu_R$ , where  $\nu_R$  is a vibrational frequency of the molecules in the sample. The redshifted light  $\nu_S$  is known as Stokes radiation, while blueshifted light  $\nu_{AS}$  is anti-Stokes radiation. Since at thermal equilibrium most of the population is at the lowest energy levels, the Stokes component is much more intense than the anti-Stokes component, which is why Stokes photons are typically detected in RS microscopy. Since a molecular/solid sample has several vibrational modes, the RS spectrum consists of discrete bands that altogether provide a chemically specific signature that allows material identification and characterization. The main drawback of this technique is the very small cross section of the RS process, as only one over  $10^9 - 10^{12}$  photons is scattered.

RS microscopy is typically performed in a point scanning fashion, whereby the illumination beam is tightly focused on the sample and scanned across the field of view (FOV), while the

forward or backward scattered Stokes light, spectrally filtered from the illumination, is measured by a frequency-domain spectrometer consisting of a dispersive element (such as a diffraction grating) coupled to an array of detectors. This approach, although well established, suffers from two drawbacks: (i) the weak RS signal results in pixel dwell times of the order of 0.1–1 s, making the acquisition of large RS images with high spatial resolution impractically long; (ii) the presence, in many samples, of an intense fluorescence background (such as, e.g., from endogenous fluorophores in cells/tissues [3]), which is also redshifted with respect to the illumination and overlaps with, and in some cases overwhelms, the RS signal.

Alternatively, the RS spectrum can be detected in the time domain using a Fourier-transform (FT) approach. In FT spectroscopy, an optical waveform is split by an interferometer into two delayed replicas, whose interference pattern is measured by a detector as a function of their relative delay. According to the Wiener–Khinchin theorem, the FT of the resulting interferogram provides the intensity spectrum of the waveform [4]. The FT approach is widely used in FTIR spectroscopy to measure absorption spectra in the mid-infrared (MIR) spectral range ( $\sim 2.5 - 25 \mu\text{m}$  wavelength) [5]. FTIR spectroscopy directly

measures the absorption of vibrational transitions, which involve a change in the dipole moment (so-called IR-active modes). It is worth noting that, while the selection rules for IR and Raman active transitions are different and (generally) complementary, both yield comparable spectroscopic information in the range of  $500\text{ cm}^{-1}$  and  $3200\text{ cm}^{-1}$ . However, the long IR wavelengths and low numerical aperture of IR objectives typically limit the spatial resolution of FTIR to  $4 - 5\text{ }\mu\text{m}$ . On the other hand, RS provides very good spatial resolution, as it makes use of visible or near-IR light, which can be focused to diffraction-limited spots of  $500\text{ nm}$  or smaller. Moreover, RS makes it easier to study biological samples, as it is free of a strong water absorption signal, which affects FTIR measurements [6]. Finally, detectors in the MIR spectral range, typically based on mercury cadmium telluride (HgCdTe), have, due to the low energy gap, high noise even at cryogenic temperatures, so that multichannel detectors have low performance, and high cost; RS, on the other hand, requires detectors based on silicon or InGaAs, which are easier to operate.

FT detection has been successfully applied to Raman spectroscopy using near-IR illumination to minimize sample fluorescence [7,8], until the diffusion of efficient CCD detectors, which facilitated dispersive approaches [9]. FT-Raman has also been exploited for point-scanning RS microscopy but without significant improvement in acquisition times over the standard dispersive techniques [10].

To increase the acquisition speed in RS microscopy, it is possible to use a wide-field configuration, in which a large area of the sample is illuminated, and the RS spectrum is measured simultaneously for all pixels of a two-dimensional (2D) detector. Wide-field Raman imaging is a particular implementation of hyperspectral (HS) imaging, an experimental approach in which a spectrum is obtained for each point of the FOV. HS imaging is a powerful tool for characterizing the composition of a variety of systems and finds a broad range of applications, from remote sensing [11] to microscopy [12,13]. However, while the technology for remote HS imaging has reached a high level of maturity, few implementations of HS microscopy have been reported so far, due to the strict requirements in terms of sensitivity, stability, and compactness. HS microscopes adopt two spectral selectivity strategies [14–16].

- (i) Bandpass approaches, in which the image is acquired at a discrete number of frequencies, by either a mosaic of bandpass filters on the detector surface [14], or a tunable spectral filter in front of a monochrome imaging camera [16–22]. Alternatively, for the specific case of RS imaging, the spectrum can be recorded by tuning the illumination frequency while keeping the narrowband detection frequency fixed [23]. Since the spectrum is measured just at a few discrete frequencies, these techniques are more accurately referred to as multispectral microscopy.
- (ii) Dispersive approaches that use spectrometers to record continuous spectra. As such, these methods are referred to as HS microscopy (HSM). In the line-scanning or push-broom approach, the illumination beam is focused along a line of the FOV and the collected signal (reflectance, fluorescence, or RS) is dispersed by a spectrometer, producing a 2D image in which one axis corresponds to the spectrum and the other to one spatial dimension [22,24,25]; the HS image is recorded by sweeping the line across the FOV. Despite increasing the acquisition speed compared to point scanning, dispersive

line-scanning approaches suffer from high losses introduced by the entrance slit of the spectrometer.

Time-domain FT detection, on the other hand, ideally lends itself to HSM. When the detector is a 2D matrix of sensors, the FT approach can be applied to each of its pixels in parallel, enabling the recording of the spectra of all pixels within a 2D FOV. Thus, FT detection can be used in imaging systems, combining wide-field microscopy and HS resolution. FT-HSM provides unique advantages over traditional methods: (i) it has higher throughput, due to the absence of filters and slits (the Jacquinot étendu advantage [26]); (ii) it can record the spectrum of a large number of pixels, due to the parallel acquisition approach, in which measurement time does not depend on the number of sampled pixels. These advantages make FT-HSM a powerful alternative to dispersive frequency-domain approaches.

Despite the enormous potential, FT-HSM must meet two challenging requirements: (i) the relative delay of the replicas must be controlled to a small fraction of the optical cycle; (ii) the beam of rays forming the interferogram at a given pixel must have a limited variation in phase-delay to add up coherently and generate interference fringes with high visibility. The first requirement calls for ultrastable interferometers, a technological challenge that explains the very limited number of FT-HSM schemes demonstrated so far. Wadduwage [27] and Müller [28] have proposed FT-HSMs for RS imaging based on proprietary interferometers. Yet, both systems are cumbersome and difficult to operate in routine experiments. Jullien [29], on the other hand, used a common-path interferometer based on a liquid crystal cell; however, this system limits the replica delay to  $130\text{ fs}$ , which corresponds to a spectral resolution of  $130\text{ cm}^{-1}$ , insufficient for RS microscopy.

Recently, we have developed a compact and ultrastable common-path birefringent interferometer [30], which we call a translating-wedge-based identical pulses encoding system (TWINS). The interferometer, briefly described in Supplement 1 and schematically sketched in the inset of Fig. 1, provides delays of hundreds of optical cycles between the two orthogonal polarizations of a light beam. Since the two fields share a common optical

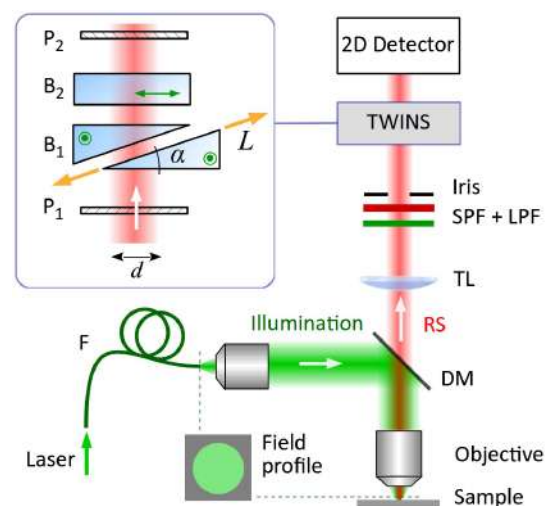


**Fig. 1.** Schematic setup of the FT-HSM, with the TWINS interferometer in the detection path;  $P_{1/2}$ , linear polarizers;  $B_{1/2}$ , birefringent blocks, whose optical axes are represented by green circles and double-arrow; F, multimode fiber; DM, dichroic mirror; RS, Raman scattering; TL, tube lens; SPF, short-pass filter for the suppression of fluorescence; LPF, long-pass filter for rejection of illumination light.

path, their delay can be adjusted with interferometric precision and exceptionally high long-term stability [31]. The TWINS interferometer, which combines the advantages of FT spectroscopy with the robustness and accuracy of a common-path design, has been employed as an FT spectrometer in spectral ranges from the visible [32] to the MIR [33], with both coherent and incoherent light beams. The TWINS system has been applied to excitation-emission spectroscopy [32,34]. It also enabled the implementation of a high-performance HS camera [35,36] and of wide-field FT-HSM [37–39], capable of simultaneous transmission and fluorescence imaging with spatial resolution  $<1 \mu\text{m}$ .

Here, we introduce a wide-field multimodal FT-HSM that allows one to acquire simultaneously, and to separate, RS and fluorescence images from the same FOV. The high throughput and stability of the TWINS interferometer enable the detection of even weak signals. Along with multimodality, a remarkable advantage of our system is the intrinsic decoupling of the Raman signal from fluorescence, a background that may limit or hinder Raman data collection. To demonstrate the performances of our system, we acquire high spatial resolution Raman images of plastic microbeads at a pixel dwell time that is one to two orders of magnitude lower than in point scanning schemes, as well as multimodal images of a multilayer-WSe<sub>2</sub> sample.

## 2. MICROSCOPE DESIGN

Figure 1 shows a schematic of the wide-field HSM setup. The system is based on a commercial optical microscope (Leica DMRBE). The illumination is a frequency-doubled Nd:YAG laser at  $\lambda = 532 \text{ nm}$  (NPS, Bright Solutions), coupled to the microscope via an optical fiber. The beam is focused by an infinity-corrected objective, and the backscattered redshifted fluorescence/Raman light is transmitted by a dichroic mirror (Semrock Di02-R532-25x36) and imaged on the 2D detector (EMCCD camera, ANDOR Luca-R, Oxford Instruments, Ireland) by a tube lens with  $f = 250 \text{ mm}$  focal length; the TWINS interferometer is placed between the tube lens and the detector. The EMCCD camera has  $1004 \times 1002$  pixels, low dark ( $0.17 \text{ e}^-/\text{px/s}$ ) and readout ( $18 \text{ e}^-/\text{px/s}$ ) noise, an effective dynamic range close to 11 bits, and 60% quantum efficiency in the spectral range of interest. It is also possible to control the gain of the EMCCD; however, for the measurements presented in this paper, the gain was set to one. A 532 nm long-pass filter (LPF) (Semrock LP03-532RU-25) is used to reject most of the residual illumination light. It is possible to further reduce the detected bandwidth by adding LPFs and short-pass filters (SPFs) in the collection path, as will be detailed later.

### A. Birefringent Interferometer

We designed the birefringent interferometer to maximize the spectral resolution for RS microscopy. In general, the spectral resolution  $\Delta\nu$  of an FT spectrometer is inversely proportional to the maximum delay  $T_{\text{max}}$  between signal replicas. For the TWINS,  $T_{\text{max}}$  depends on three parameters: crystal birefringence  $\Delta n = n_o - n_e$ , wedge apex angle  $\alpha$ , and maximum translation length  $L$ , according to the expression

$$T_{\text{max}} = \frac{L}{c} \Delta n \sin \alpha. \quad (1)$$

Equation (1) shows that large delays require high birefringence and long translations. By comparing the optical properties

of the most common visible birefringent materials (see list in Supplement 1), YVO<sub>4</sub> represents the best compromise among transparency range, birefringence, and strength of the refractive index. This last parameter is particularly important because it is responsible for the beam deviation caused by each wedge (which acts like a prism). In fact, along with the non-uniform phase difference of a pencil of rays after propagating inside the interferometer [37], a large beam deviation introduces a spatial walk-off between the signal replicas, leading to a reduction of the interferometric contrast. We hence opted for YVO<sub>4</sub>, which has lower values of  $n_o/e$  with respect, e.g., to the highly birefringent TiO<sub>2</sub>. The interferometric contrast experimentally reached with the YVO<sub>4</sub> TWINS in the microscope is 55%, in agreement with the estimation proposed in [37]. Due to its broad transparency range, YVO<sub>4</sub> can be used to detect RS with illumination wavelength broadly tunable from the visible to the IR, which can be selected depending on the sample being examined.

The chosen wedges' tip angle is  $\alpha = 10^\circ$ , and their transverse size is 30 mm, limited by technical constraints in growing the crystal. The wedge scan is performed with a stepper motor (25 mm travel range, 0.02  $\mu\text{m}$  step size); since the image beam has a diameter  $d = 12 \text{ mm}$  at the wedge plane, the maximum excursion of the wedges without clipping the image is 18 mm. This corresponds to a maximum delay range of 2930 fs at 600 nm, which leads to a spectral resolution of  $21 \text{ cm}^{-1}$ .

### B. Top-Hat Illumination

To provide uniform illumination of the sample FOV for wide-field imaging, we used a multimode, large-core fiber, the tip of which is imaged on the sample surface [see Fig. 1(a)]. To guarantee a flat-field profile at the fiber tip, a mechanical scrambler distributes the modes in the core of the fiber. This latter is also shaken by a vibrating voice coil to average out the speckle pattern at the sample surface induced by the spatial coherence of the monochromatic laser beam. The illumination spot at the sample plane is a flat circular field, whose diameter covers 82% of the FOV width; since both the illumination light and signal propagate through the same objective, this ratio holds true for any magnification. Details on the characterization of the top-hat illumination are reported in Supplement 1.

### C. Sampling Strategy

FT spectroscopy, which measures a time-domain interferogram, offers a great advantage over dispersive spectrometers because it provides access to different features of the spectrum by tailoring the sampling strategy. For example, in [37], we developed a sampling procedure that synthesizes a tunable spectral filter. The sampling of the interferogram is defined by two parameters: *scan range*  $T$  and *sampling period*  $T_s$ . The scan range, defined as  $T = |T_2 - T_1|$ , where  $T_1$  ( $T_2$ ) is the initial (final) delay of the interferogram, is inversely proportional to the spectral resolution  $\Delta\nu$  of the interferometer. Additionally, the proper choice of  $T_1$  and  $T_2$  enables selecting the fluorescence or the Raman signals: it is on this unique advantage that our multimodal microscope is based. To illustrate the method, we recall two properties of the FT.

- (i) The bandwidth of an optical signal is inversely proportional to the duration of the corresponding interferogram. As a consequence, the interferogram produced by a broadband signal has



significantly fewer optical cycles than the one of a narrowband field.

- (ii) The FT is a linear operator; hence the interferogram of a linear combination of uncorrelated spectra is the linear superposition of individual interferograms.

These properties can be used to decompose a spectrum into its broadband and narrowband components, according to the approach illustrated in Fig. 2. Figure 2(a) shows a multimodal spectrum consisting of narrow features (e.g., Raman peaks) overlapped to a broad background (e.g., fluorescence). The corresponding interferogram is given in (b). It is characterized by large oscillations at early delays and tiny signals at long delays, whereas its average value  $C$  is proportional to the integrated spectrum. The signal at short delays corresponds mostly to the broad spectral features, while the oscillations at long delays are due only to the narrowband components. One can therefore separate these signals by taking the FT of the symmetric early-delay interferogram (red dashed box) or of the long-lived oscillation. In the latter case, we consider only the portion of the interferogram at large positive delays (green dashed window). Figure 2(c) shows the resulting spectra, which correspond to the broadband and narrowband components of the initial spectrum, which are now completely separated. This method allows the extraction of fluorescence-free Raman spectra and offers an additional advantage: since the scan does not include the strongly oscillating interferogram at early delays, the long-lived oscillations can be obtained with a longer integration time without saturating the detector dynamic range.

It must be noted that in practice, this method is advantageous only in an FT-based detection system, as in the case of our FT-HSM. Conversely, the application of the same time-filtering approach to the numerical FT of a measured frequency-domain spectrum would lead to a severe degradation of the retrieved peaks.

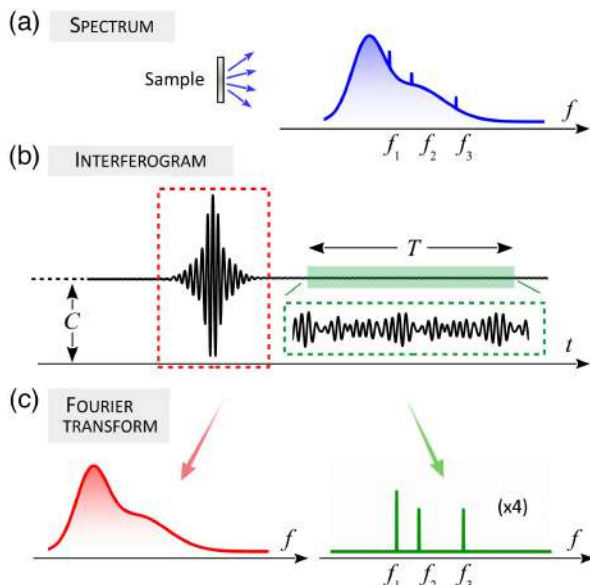


**Fig. 2.** Schematic representation of the FT approach in the case of a multimode spectrum, (a) characterized by both broadband (e.g., fluorescence) and narrowband (e.g., Raman peaks) features. (b) Corresponding interferogram, characterized by the overlap of prominent few-cycle oscillations at early delays and weaker signals lasting for a large number of cycles. (c) The application of FT to the early delay fraction of the interferogram conveys the broadband, slowly varying spectrum; the long-lasting oscillations at long delays give rise to narrowband spectra.

The second relevant acquisition parameter is the sampling period  $T_s$ , which, besides total acquisition time, also influences the signal-to-noise ratio (SNR) of the measurements, as explained in Supplement 1. The proper  $T_s$  is hence a trade-off between these two parameters, and depends on the system under test. In the following sections, we will present two application examples of our Raman microscope in which the sampling strategy is adapted to the signal strength.

### 3. RESULTS AND DISCUSSION

#### A. Raman Measurement

To test the Raman FT-HSM we measured a mixture of polymethyl-methacrylate (PMMA) and polystyrene (PS) beads, respectively, of  $\sim 8 \mu\text{m}$  and  $\sim 10 \mu\text{m}$  diameter, air-dried on a microscope steel slide (see Supplement 1 for details on sample preparation). For this measurement, we added in the detection path a 550 nm LPF (Thorlabs FELH0550) and a 650 nm SPF (Thorlabs FESH0650): they reject the residual illumination light and block the background outside the Raman bands of interest, tailoring the detection bandwidth to the expected Raman-shift range. Narrowing the detection bandwidth has two advantages. First, it reduces the total amount of collected background, hence lowering the average value  $C$  of the interferogram measured for each pixel (see Fig. 2); this enables better use of the sensor's dynamic range. Second, it allows for sampling beyond the Nyquist-Shannon (NS) limit without the risk of spectral aliasing, as discussed in Supplement 1.

With the selected LPF/SPF filters, the detection band is in the frequency range from  $\nu_{\min} \approx 460 \text{ THz}$  to  $\nu_{\max} \approx 545 \text{ THz}$  (corresponding to Raman shifts from  $615 \text{ cm}^{-1}$  to  $3412 \text{ cm}^{-1}$ ): the sampling step can hence be increased to  $T_s = 3 \text{ fs}$  at 600 nm, which is  $\sim 3$  times larger than the NS limit ( $T_s < 1 \text{ fs}$ ), and the acquisition time can be reduced accordingly. The scan delay ranged from  $T_1 = 34 \text{ fs}$  to  $T_2 = 2452 \text{ fs}$  at 600 nm, where the starting delay  $T_1$  excludes the oscillating contribution of the broadband background, whereas  $T_2$  is the maximum delay allowed by the YVO<sub>4</sub> TWINS. This delay range corresponds to a spectral resolution of  $23 \text{ cm}^{-1}$ . By applying the undersampling approach, the whole scan consists of 806 frames.

We used a 20 $\times$  objective (Leica PL FLUOTAR, 20 $\times$ , NA 0.40), which leads to an illumination spot on the object plane with a diameter of  $320 \mu\text{m}$ . The laser power was set to 350 mW, corresponding to an irradiance on the sample of  $435 \text{ W/cm}^2$ . We used a hardware  $2 \times 2$  pixel binning, resulting in images with  $502 \times 501$  pixels. Since the size of the binned pixels is comparable to the Abbe's limit of the microscope, binning does not affect the spatial resolution, but increases the SNR for a given measurement time. The integration time of each frame was 2.5 s, and the total measurement time, including communication time with the motor and camera, was 38 min. For the sake of comparison, in a raster-scanning approach, such an acquisition time would correspond to a pixel dwell time of 8 ms, resulting in unacceptably low SNR for RS spectra.

After the acquisition, the temporal hypercube ( $502 \times 501 \times 806$ ) was transformed into a spectral hypercube by performing the FT at each pixel. The hypercube was then processed using the RamApp software [40] following two different techniques in sequence. By applying the mini-batch k-means analysis [41], we identified the substrate (i.e., the steel slide and the area outside the

illumination) and the sample areas. The centroid spectra related to the PS and PMMA clusters identified with this method are shown in Supplement 1. Subsequently, we performed the multivariate curve resolution (MCR) analysis [42] on the sample points: the results are shown in Fig. 3. The spectra of the first two MCR components [see Fig. 3(a)] match the Raman signatures of PS and PMMA and are in very good agreement with the peaks recorded by a standard RS system (home-built system using a 660 nm illumination laser and standard spectrometer; see Supplement 1). Note that, due to our acquisition approach, the spectra are background-free, as illustrated in Section 2.C and Fig. 2. The FWHM of the isolated peaks is  $23\text{ cm}^{-1}$ , in agreement with the spectral resolution expected from the scanning range and the apodization of the interferograms (see Supplement 1 for details on the apodization); the resolution is sufficient to separate the characteristic peaks of the two species. The MCR analysis also enables us to distinguish the two types of beads, as illustrated in Figs. 3(c)–3(e).

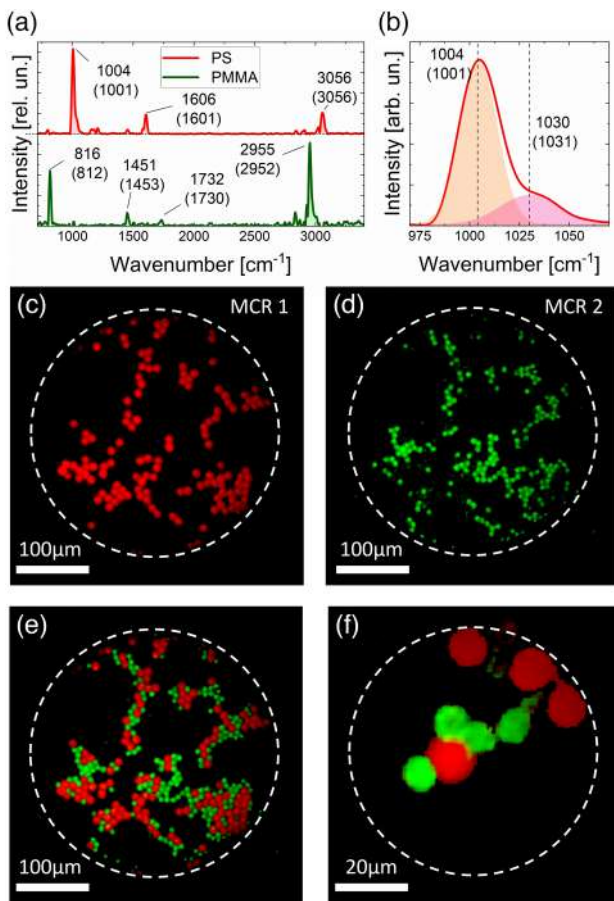


**Fig. 3.** Wide-field Raman HSM of polymer beads. (a) Spectra of the first (PS) and second (PMMA) components retrieved with MCR analysis; for the main peaks, we provide the positions measured both with our system and with a standard Raman spectrometer (in brackets); complete spectral comparison in Supplement 1. (b) Detail of the  $1004\text{-cm}^{-1}$  peak of PS (solid red line), together with the fitting Gaussian curves (shaded areas). The frequencies of the fitting maxima are shown by labels (RS peak values in brackets). (c) Map of the first MCR component (PS); the white dashed circumference identifies the illuminated area of the sample. (d) Map of the second MCR component (PMMA). (e) Composite map retrieved by merging the MCR images in (c) and (d). (f) Composite MCR map of Raman map obtained with  $100\times$  magnification. Sampling: the same as for the  $20\times$  acquisition; binning:  $6 \times 6$ ; integration time: 2 s.

To resolve the two nearby Raman modes of PS at  $1001\text{ cm}^{-1}$  and  $1030\text{ cm}^{-1}$  [see Fig. 3(b)], we fitted the spectrum with two Gaussian functions using the nonlinear least-squares Levenberg–Marquardt method: the free parameters of the interpolation were the amplitudes, central frequencies, and FWHM. The retrieved FWHM is  $22\text{ cm}^{-1}$  for the peak at  $1004\text{ cm}^{-1}$  and  $34\text{ cm}^{-1}$  for the peak at  $1030\text{ cm}^{-1}$ : the position and FWHM of the fitting peaks are in good agreement with the expected values. We repeated the measurement using a  $100\times$  objective (Leica PL FLUOTAR,  $100\times$ , NA 0.75), which scales down the image FOV to  $64\text{ }\mu\text{m}$ ; the laser power on the sample was reduced to  $70\text{ mW}$  (irradiance  $2175\text{ W/cm}^2$ ) to prevent sample damage, and the total acquisition time was 29 min. The clustered image after MCR analysis is shown in Fig. 3(f).

## B. Multimodal Acquisition

To demonstrate the multimodal capability of our microscope, we analyzed a multilayer sample of the transition metal dichalcogenide (TMD)  $\text{WSe}_2$ , acquiring both fluorescence and Raman HS images. TMDs are van der Waals semiconductors made of atomically thin layers with strong in-plane covalent bonds, stacked together by weak out-of-plane forces [43]. This allows the separation of individual monolayers (1L) from multilayers using mechanical exfoliation [44]. When the system thickness undergoes a transition from multilayer to 1L, the quantum confinement experienced by the electrons in the out-of-plane direction radically modifies the band structure of the material, switching from indirect to direct bandgap, as evidenced by the increase of the fluorescence quantum yield in 1Ls, as compared to bilayers (2Ls) [45].

We tested a large area TMD device fabricated using the gold-assisted mechanical exfoliation technique [46]. This method can produce 1L-TMDs of mm size, but with the drawback of a low spatial homogeneity of the optical properties, with areas covered not only by 1L regions, but also by 2Ls or multilayers, demanding the use of wide-field characterization techniques for their identification [39,47]. The sample preparation methodology and its reflectivity image are provided in Supplement 1. For all spectral measurements, we used a  $20\times$  objective (Leica PL FLUOTAR,  $20\times$ , NA 0.40). Although the system is in principle able to measure simultaneously the RS and the fluorescence spectra, we performed two sequential measurements adjusting the acquisition parameters (sampling period and exposure time; see table in Supplement 1) to allow separation of the RS and fluorescence contributions.

Since in multilayer  $\text{WSe}_2$  both fluorescence and Raman signals are very weak, we applied hardware binning. Moreover, to obtain acceptable SNR for the Raman measurement, the sampling step was lowered to  $T_s = 0.813\text{ fs}$  at  $600\text{ nm}$ , significantly shorter than the sampling used for the PS/PMMA beads, and well below the NS limit. Since the multilayer  $\text{WSe}_2$  has lower Raman shifts with respect to PS/PMMA beads, the filters in the detection path were changed to a  $532\text{ nm}$  LPF (Semrock LP03-532RU-25) and a  $600\text{ nm}$  SPF (Thorlabs FES0600), allowing one to measure Raman shifts from  $160\text{ cm}^{-1}$  up to  $2130\text{ cm}^{-1}$ .

Figure 4 shows the results of multimodal measurements. The selected area has both 1L and 2L regions (the sample micrograph is provided in Supplement 1). In the fluorescence 2D map [shown in false RGB colors in Fig. 4(a)], we can clearly discriminate the 1L (white area) from 2L (red area) regions. 1L regions are characterized by different emission intensities and slight variations of the



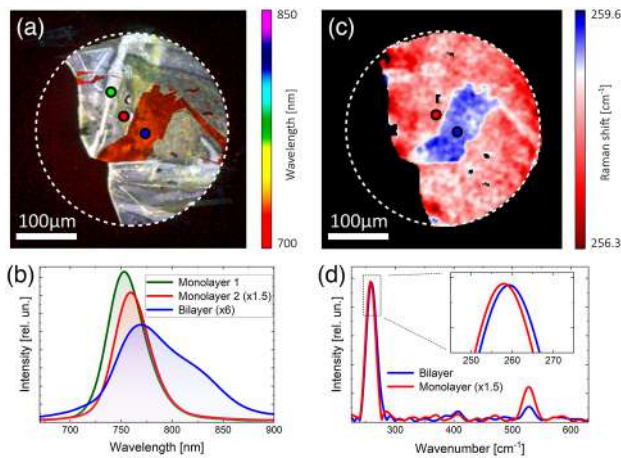


**Fig. 4.** (a) False-color RGB image obtained from the fluorescence map. The white dashed circumference identifies the illuminated area of the sample. Three circles indicate three selected regions of interest (ROIs) on 1L (green and red) and 2L (blue). (b) Fluorescence spectra of selected ROIs in (a). (c) Peak map of the  $A_{1g}$  Raman mode of  $WSe_2$ . Two circles indicate one ROI on 1L (red) and one ROI on 2L (blue). (d) Raman spectra of selected ROIs in (c). The inset shows a zoom of the peak.

peak, revealing the strong spatial heterogeneity of the sample [46]. The corresponding fluorescence spectra are shown in Fig. 4(b). The peaks originate from the radiative emission of the neutral A exciton [48,49]. The peak positions of 1L at  $\sim 750$  nm and of 2L at  $\sim 775$  nm are in good agreement with previous results [48,49].

As expected, 2L displays a weaker fluorescence intensity with respect to 1L, due to the transition from direct to indirect bandgap. On the other hand, the variations in the spectra from 1L regions can result from fluctuations in dielectric environment [50], strain-induced electronic bandgap shifts [51], and electrostatic potentials [52]. 1L-TMDs are very flexible, being atomically thin, and they withstand large strain levels ( $>10\%$ ) before fracture, which can also modify their electronic band structure and shift the excitons' fluorescence spectra [53]. Strained regions in 1L-TMDs can occur during the fabrication process, as in our case, or can be intentionally introduced by tailored substrates [54], thus achieving a continuously controlled bandgap modification. Our technique helps to identify the highly strained regions in the observed samples. In some cases, the strain level in 2Ls is high enough that a strong modification of the band structure occurs, leading to a shift from indirect to direct bandgap. The fluorescence intensity increases accordingly, becoming comparable to the one of the unstrained 1L [55]. In this case, Raman measurements can be very helpful to distinguish 1L from 2L.

The RS spectra [Fig. 4(d)] clearly identify the out-of-plane  $A_{1g}$  optical phonon mode of  $WSe_2$ , degenerate with the  $E_{2g}$  mode, at  $258\text{ cm}^{-1}$  [56]. Instead, the peak at  $525\text{ cm}^{-1}$  originates from the underlying silicon substrate. Figure 4(c) shows the map of the  $A_{1g}$  peak in which we are able to resolve a Raman-shift variation in the 2L of  $\sim 3\text{ cm}^{-1}$ , in agreement with previous results [57–59]. Such precision is possible because, even if the spectral resolution of the HSM is  $23\text{ cm}^{-1}$ , the spectral-peak maximum in each pixel of the image can be localized with a precision of  $\sim 1\text{ cm}^{-1}$ . This feature stems from the high SNR of the measurements and the exceptional stability of the TWINS interferometer, which guarantees jitter-free spectra.

## 4. CONCLUSIONS

In this work, we have introduced a wide-field FT Raman microscope that acquires high spatial resolution maps in a significantly shorter time compared to state-of-the-art point-scanning Raman microscopes, with accurate RS peak separation. The FT approach allows us to select the best sampling strategy according to the specific measurement: we can retrieve background-free maps and significantly reduce the acquisition time by adopting appropriate sampling strategies. By measuring PMMA and PS beads, we show outstandingly short Raman acquisition time ( $\sim 38$  min for a 250 kpixel map) and demonstrate the capability of the microscope to identify the chemical composition of small plastic beads ( $<10\text{ }\mu\text{m}$  diameter) based on their Raman spectra. We demonstrate its multimodal capabilities by acquiring in sequence Raman and fluorescence maps for the same FOV on a  $WSe_2$  sample in the presence of both 1L and 2L regions. In this case, the multimodality of our microscope allows us to combine information on sample heterogeneity obtained from fluorescence data with the identification of 1L and 2L provided by the Raman signal.

The spectral resolution of the Raman HSM is  $23\text{ cm}^{-1}$ ; it can be further improved by developing a TWINS interferometer with a longer maximum delay scan. Moreover, after suitable optimization, the system can be applied also to the study of biological samples. Here, the main challenge concerns the minimization of sample heating, arising from the inefficient monodirectional dissipation of the excess power conveyed to a widely illuminated area. Sample heating can be reduced by utilizing longer illumination wavelengths (e.g., 785 nm), thus lowering the power absorption, or by developing suitable heat dissipation strategies. Finally, we point out that the simple design of our Raman HSM, which is based on a standard optical microscope coupled to our compact ultrastable TWINS interferometer and a suitable illumination system, could facilitate its further development into a commercial product.

**Funding.** HORIZON EUROPE Marie Skłodowska-Curie Actions (101066108); H2020 Marie Skłodowska-Curie Actions (ENOSIS H2020-MSCA-IF-2020-101029644); National Science Foundation (DMR-2011738).

**Acknowledgment.** X.Z. acknowledges support for 2D sample preparation by the Materials Science and Engineering Research Center (MRSEC) through NSF A.G. and G.C. acknowledge support by the European Union Marie Skłodowska-Curie Actions project ENOSIS. C.T. and G.C. acknowledge support by European Union's Horizon Europe (HORIZON) Research and Innovation Programme under the Marie Skłodowska-Curie Action PIONEER. C.M. and R.V. acknowledge support by European Union's European Innovation Council (EIC), TROPHY PATHFINDER-OPEN-01 101047137 [60].

**Disclosures.** The authors declare no conflicts of interest.

**Data availability.** Data underlying the results presented in this paper are not publicly available at this time but may be obtained from the authors upon reasonable request.

**Supplemental document.** See Supplement 1 for supporting content.

## REFERENCES

1. S. Zhang, N. Zhang, Y. Zhao, T. Cheng, X. Li, R. Feng, H. Xu, Z. Liu, J. Zhang, and L. Tong, "Spotting the differences in two-dimensional materials—the Raman scattering perspective," *Chem. Soc. Rev.* **47**, 3217–3240 (2018).
2. R. Vanna, A. De la Cadena, B. Talone, C. Manzoni, M. Marangoni, D. Polli, and G. Cerullo, "Vibrational imaging for label-free cancer diagnosis and classification," *Riv. Nuovo Cimento* **45**, 107–187 (2022).

3. H. J. Butler, L. Ashton, B. Bird, G. Cinque, K. Curtis, J. Dorney, K. Esmonde-White, N. J. Fullwood, B. Gardner, P. L. Martin-Hirsch, M. J. Walsh, M. R. McAinsh, N. Stone, and F. L. Martin, "Using Raman spectroscopy to characterize biological materials," *Nat. Protoc.* **11**, 664–687 (2016).
4. S. Davis, M. Abrams, and J. Brault, *Fourier Transform Spectrometry* (Academic, 2001).
5. S. P. Davis, M. C. Abrams, and J. W. Brault, *Fourier Transform Spectrometry* (Elsevier, 2001).
6. I. Nottingher, J. Jones, S. Verrier, I. Bisson, P. Embanga, P. Edwards, J. Polak, and L. Hench, "Application of FTIR and Raman spectroscopy to characterisation of bioactive materials and living cells," *J. Spectrosc.* **17**, 893584 (2003).
7. D. B. Chase, "Fourier transform Raman spectroscopy," *J. Am. Chem. Soc.* **108**, 7485–7488 (1986).
8. I. W. Levin and E. N. Lewis, "Fourier transform Raman spectroscopy of biological materials," *Anal. Chem.* **62**, 1101A–1111A (1990).
9. X. Zhu, T. Xu, Q. Lin, and Y. Duan, "Technical development of Raman spectroscopy: from instrumental to advanced combined technologies," *Appl. Spectrosc. Rev.* **49**, 64–82 (2014).
10. M. Baranska, H. Schulz, P. Rösch, M. A. Strehle, and J. Popp, "Identification of secondary metabolites in medicinal and spice plants by NIR-FT-Raman microspectroscopic mapping," *Analyst* **129**, 926–930 (2004).
11. R. G. Sellar and G. D. Boreman, "Classification of imaging spectrometers for remote sensing applications," *Opt. Eng.* **44**, 013602 (2005).
12. D. T. Dicker, J. M. Lerner, and W. S. El-Deiry, "Hyperspectral image analysis of live cells in various cell cycle stages," *Cell Cycle* **6**, 2563–2570 (2007).
13. T. Zimmermann, "Spectral imaging and linear unmixing in light microscopy," in *Microscopy Techniques* (Springer, 2005), pp. 245–265.
14. N. A. Hagen and M. W. Kudenov, "Review of snapshot spectral imaging technologies," *Opt. Eng.* **52**, 090901 (2013).
15. A. Hegyi and J. Martini, "Hyperspectral imaging with a liquid crystal polarization interferometer," *Opt. Express* **23**, 28742–28754 (2015).
16. M. Dickinson, G. Bearman, S. Tille, R. Lansford, and S. Fraser, "Multi-spectral imaging and linear unmixing add a whole new dimension to laser scanning fluorescence microscopy," *Biotechniques* **31**, 1272–1278 (2001).
17. A. Raz and D. Mendlovic, "Sequential filtering for color image acquisition," *Opt. Express* **22**, 26878–26883 (2014).
18. G. Lu and B. Fei, "Medical hyperspectral imaging: a review," *J. Biomed. Opt.* **19**, 010901 (2014).
19. S. Yang, B. Li, A. Akkus, O. Akkus, and L. Lang, "Wide-field Raman imaging of dental lesions," *Analyst* **139**, 3107–3114 (2014).
20. A. Papour, J. H. Kwak, Z. Taylor, B. Wu, O. Stafsudd, and W. Grundfest, "Wide-field Raman imaging for bone detection in tissue," *Biomed. Opt. Express* **6**, 3892–3897 (2015).
21. H. R. Morris, C. C. Hoyt, and P. J. Treado, "Imaging spectrometers for fluorescence and Raman microscopy: acousto-optic and liquid crystal tunable filters," *Appl. Spectrosc.* **48**, 857–866 (1994).
22. S. Schlücker, M. D. Schaeberle, S. W. Huffman, and I. W. Levin, "Raman microspectroscopy: a comparison of point, line, and wide-field imaging methodologies," *Anal. Chem.* **75**, 4312–4318 (2003).
23. H. Li, W. Luo, G. Li, G. Zhang, P. Zhang, C. Li, and Y. Gu, "A practical wide-field Raman imaging method with high spectral and spatial resolution," *Rev. Sci. Instrum.* **89**, 083103 (2018).
24. S. Ortega, R. Guerra, M. Diaz, H. Fabelo, S. López, G. M. Callico, and R. Sarmiento, "Hyperspectral push-broom microscope development and characterization," *IEEE Access* **7**, 122473 (2019).
25. Q. Li, Y. Xue, G. Xiao, and J. Zhang, "Study on microscope hyperspectral medical imaging method for biomedical quantitative analysis," *Chin. Sci. Bull.* **53**, 1431–1434 (2008).
26. P. Jacquinot, "New developments in interference spectroscopy," *Rep. Prog. Phys.* **23**, 267 (1960).
27. D. N. Wadduwage, V. R. Singh, H. Choi, Z. Yaqoob, H. Heemskerk, P. Matsudaira, and P. T. So, "Near-common-path interferometer for imaging Fourier-transform spectroscopy in wide-field microscopy," *Optica* **4**, 546–556 (2017).
28. W. Müller, M. Kielhorn, M. Schmitt, J. Popp, and R. Heintzmann, "Light sheet Raman micro-spectroscopy," *Optica* **3**, 452–457 (2016).
29. A. Jullien, R. Pascal, U. Bortolozzo, N. Forget, and S. Residori, "High-resolution hyperspectral imaging with cascaded liquid crystal cells," *Optica* **4**, 400–405 (2017).
30. C. A. Manzoni, D. Brida, and G. N. F. Cerullo, "Phase-locked delay device including an optical wedge pair," US Patent 9,182,284 (10 November 2015).
31. D. Brida, C. Manzoni, and G. Cerullo, "Phase-locked pulses for two-dimensional spectroscopy by a birefringent delay line," *Opt. Lett.* **37**, 3027–3029 (2012).
32. A. Perri, F. Preda, C. Dandrea, E. Thyryhaug, G. Cerullo, D. Polli, and J. Hauer, "Excitation-emission Fourier-transform spectroscopy based on a birefringent interferometer," *Opt. Express* **25**, A483–A490 (2017).
33. J. Réhault, M. Maiuri, C. Manzoni, D. Brida, J. Helbing, and G. Cerullo, "2D IR spectroscopy with phase-locked pulse pairs from a birefringent delay line," *Opt. Express* **22**, 9063–9072 (2014).
34. E. Thyryhaug, S. Krause, A. Perri, G. Cerullo, D. Polli, T. Vosch, and J. Hauer, "Single-molecule excitation-emission spectroscopy," *Proc. Natl. Acad. Sci. USA* **116**, 4064–4069 (2019).
35. A. Perri, B. N. de Faria, D. T. Ferreira, D. Comelli, G. Valentini, F. Preda, D. Polli, A. De Paula, G. Cerullo, and C. Manzoni, "Hyperspectral imaging with a TWINS birefringent interferometer," *Opt. Express* **27**, 15956–15967 (2019).
36. A. Candeo, B. Ardini, M. Ghirardello, G. Valentini, L. Clivet, C. Maury, T. Calligaro, C. Manzoni, and D. Comelli, "Performances of a portable Fourier transform hyperspectral imaging camera for rapid investigation of paintings," *Eur. Phys. J. Plus* **137**, 1–13 (2022).
37. A. Candeo, B. N. de Faria, M. Erreni, G. Valentini, A. Bassi, A. De Paula, G. Cerullo, and C. Manzoni, "A hyperspectral microscope based on an ultrastable common-path interferometer," *APL Photon.* **4**, 120802 (2019).
38. C. A. Manzoni, G. Cerullo, D. Polli, A. Perri, F. Preda, G. Valentini, and A. Bassi, "Fourier-transform hyperspectral imaging system," US Patent 11,346,719 B2 (31 May 2022).
39. C. Trovatiello, A. Genco, C. Cruciano, B. Ardini, Q. Li, X. Zhu, G. Valentini, G. Cerullo, and C. Manzoni, "Hyperspectral microscopy of two-dimensional semiconductors," *Opt. Mater. X* **14**, 100145 (2022).
40. <https://ramapp.io/>
41. D. Sculley, "Web-scale k-means clustering," in *19th International Conference on World Wide Web* (2010), p. 1177–1178.
42. A. De Juan, J. Jaumot, and R. Tauler, "Multivariate curve resolution (MCR): solving the mixture analysis problem," *Anal. Methods* **6**, 4964–4976 (2014).
43. K. F. Mak, C. Lee, J. Hone, J. Shan, and T. F. Heinz, "Atomically thin MoS<sub>2</sub>: a new direct-gap semiconductor," *Phys. Rev. Lett.* **105**, 136805 (2010).
44. K. S. Novoselov, D. Jiang, F. Schedin, T. Booth, V. Khotkevich, S. Morozov, and A. K. Geim, "Two-dimensional atomic crystals," *Proc. Natl. Acad. Sci. USA* **102**, 10451–10453 (2005).
45. K. F. Mak and J. Shan, "Photonics and optoelectronics of 2D semiconductor transition metal dichalcogenides," *Nat. Photonics* **10**, 216–226 (2016).
46. F. Liu, W. Wu, Y. Bai, S. H. Chae, Q. Li, J. Wang, J. Hone, and X.-Y. Zhu, "Disassembling 2D van der Waals crystals into macroscopic monolayers and reassembling into artificial lattices," *Science* **367**, 903–906 (2020).
47. T. Severs Millard, A. Genco, E. M. Alexeev, S. Randerson, S. Ahn, A. Jang, H. S. Shin, and A. I. Tartakovskii, "Large area chemical vapour deposition grown transition metal dichalcogenide monolayers automatically characterized through photoluminescence imaging," *npj 2D Mater. Appl.* **4**, 1–9 (2020).
48. T. Yan, X. Qiao, X. Liu, P. Tan, and X. Zhang, "Photoluminescence properties and exciton dynamics in monolayer WSe<sub>2</sub>," *Appl. Phys. Lett.* **105**, 101901 (2014).
49. M. Rahaman, O. Selyshchev, Y. Pan, R. Schwartz, I. Milekhin, A. Sharma, G. Salvan, S. Gemming, T. Korn, and D. R. T. Zahn, "Observation of room-temperature dark exciton emission in nanopatch-decorated monolayer WSe<sub>2</sub> on metal substrate," *Adv. Opt. Mater.* **9**, 2101801 (2021).
50. A. Raja, L. Waldecker, J. Zipfel, Y. Cho, S. Brem, J. D. Ziegler, M. Kulig, T. Taniguchi, K. Watanabe, E. Malic, T. F. Heinz, T. C. Berkelbach, and A. Chernikov, "Dielectric disorder in two-dimensional materials," *Nat. Nanotechnol.* **14**, 832–837 (2019).
51. B. G. Shin, G. H. Han, S. J. Yun, H. M. Oh, J. J. Bae, Y. J. Song, C.-Y. Park, and Y. H. Lee, "Indirect bandgap puddles in monolayer MoS<sub>2</sub> by substrate-induced local strain," *Adv. Mater.* **28**, 9378–9384 (2016).
52. J. Xue, J. Sanchez-Yamagishi, D. Bulmash, P. Jacquod, A. Deshpande, K. Watanabe, T. Taniguchi, P. Jarillo-Herrero, and B. J. LeRoy, "Scanning

- tunnelling microscopy and spectroscopy of ultra-flat graphene on hexagonal boron nitride," *Nat. Mater.* **10**, 282–285 (2011).
53. K. P. Dhakal, S. Roy, H. Jang, X. Chen, W. S. Yun, H. Kim, J. Lee, J. Kim, and J.-H. Ahn, "Local strain induced band gap modulation and photoluminescence enhancement of multilayer transition metal dichalcogenides," *Chem. Mater.* **29**, 5124–5133 (2017).
  54. L. Sortino, M. Brooks, P. G. Zotev, A. Genco, J. Cambiasso, S. Mignuzzi, S. A. Maier, G. Burkard, R. Sapienza, and A. I. Tartakovskii, "Dielectric nanoantennas for strain engineering in atomically thin two-dimensional semiconductors," *ACS Photon.* **7**, 2413–2422 (2020).
  55. S. B. Desai, G. Seol, J. S. Kang, H. Fang, C. Battaglia, R. Kapadia, J. W. Ager, J. Guo, and A. Javey, "Strain-induced indirect to direct bandgap transition in multilayer WSe<sub>2</sub>," *Nano Lett.* **14**, 4592–4597 (2014).
  56. H. Terrones, E. D. Corro, S. Feng, J. Poumirol, D. Rhodes, D. Smirnov, N. Pradhan, Z. Lin, M. Nguyen, A. Elas, T. E. Mallouk, L. Balicas, M. A. Pimenta, and M. Terrones, "New first order Raman-active modes in few layered transition metal dichalcogenides," *Sci. Rep.* **4**, 4215 (2014).
  57. H. Sahin, S. Tongay, S. Horzum, W. Fan, J. Zhou, J. Li, J. Wu, and F. Peeters, "Anomalous Raman spectra and thickness-dependent electronic properties of Wse<sub>2</sub>," *Phys. Rev. B* **87**, 165409 (2013).
  58. J. Kim, J.-U. Lee, and H. Cheong, "Polarized Raman spectroscopy for studying two-dimensional materials," *J. Phys. Condens. Matter* **32**, 343001 (2020).
  59. W. Zhao, Z. Ghorannevis, K. K. Amara, J. R. Pang, M. Toh, X. Zhang, C. Kloc, P. H. Tan, and G. Eda, "Lattice dynamics in mono-and few-layer sheets of WS<sub>2</sub> and WSe<sub>2</sub>," *Nanoscale* **5**, 9677–9683 (2013).
  60. <http://cordis.europa.eu/project/id/101047137>